China Instrument and Control Society
Instrumentation

OPEN ACCESS

INSTRUMENTATION, Vol. 12, No. 3, September 2025 https://doi.org/10.15878/j.instr.202500288

Article

Vibration Measurement Technology of Optical Fiber SS-Oct Based on All-Phase Fast Fourier Transform

Famin Wang[1], Yongyi Tan[1], Jingyi Gu[1], Jiao Li[2], Chi Wang[1*]

[1] School of Mechanical Engineering and Automation, Shanghai University, Shanghai 200444, China

[2] State Key Laboratory of Precision Measurement Technology and Instruments, Tianjin University, Tianjin 300072, China

[*] Corresponding author email: wangchi@shu.edu.cn

Abstract: This study utilizes the All-phase Fast Fourier Transform (FFT) spectral analysis phase difference technique combined with a Kaiser-Hanning hybrid convolution window to enhance the displacement resolution of Swept Source Optical Coherence Tomography (SS-OCT), enabling sub-nanometer level micro-vibration measurements. By employing a designed ultra-small Gradient Index (GRIN) fiber probe, the signal-to-noise ratio (SNR) is increased to 40 dB, and the frequency estimation error of the All-phase FFT phase difference method is reduced to 10^-4. An SS-OCT system incorporating the ultra-small GRIN probe is developed and applied to micro-vibration detection experiments. The system successfully captures vibration signals from a 0.8 mm diameter micro-motor shaft, showing an increase in vibration amplitude from 2 μm to 6 μm after damage. Experimental results demonstrate a displacement resolution of 1 nm under optimal conditions. These findings highlight the potential of the ultra-small GRIN fiber probe-based SS-OCT system for detecting micro-mechanical damage and the effectiveness of the All-phase FFT spectral analysis phase difference method in improving the system's displacement resolution, enabling the fiber-optic SS-OCT system to maintain sub-nanometer-level measurement precision.

Keywords: vibration monitoring; SS-OCT; grin fiber; all-phase FFT; precision

Citation: Famin Wang, Yongyi Tan, Jingyi Gu, Jiao Li, Chi Wang."Vibration Measurement Technology of Optical Fiber SS-Oct Based on All-Phase Fast Fourier Transform." Instrumentation 12, no.3 (September 2025). https://doi.org/10.15878/j.instr.202500288

1 Introduction

Optical Coherence Tomography (OCT) is an optical imaging technology based on the principle of low coherence interference. It is characterized by its non-invasive and high resolution, playing an important role in retinal imaging, macular degeneration, macular hole detection, and glaucoma detection[1-6]. Due to its excellent spatial resolution and large dynamic measurement range, OCT technology has been researched and developed in the field of micro-displacement and micro-vibration measurement in recent years[7-10]. In 2015, Zhong proposed using OCT technology for microstructure vibration detection and combined spectrum correction technology with OCT ranging technology to study high-precision Optical Coherence Vibrometer (OCV) [11]. Subsequently, the frequency estimation performance of the energy centroid method and the velocity measurement performance of the high-performance optical coherence vibrometer were analyzed and researched, further promoting the development of OCV technology[12,13]. Building upon OCV technology, Zhou et al. developed an acoustically excited frequency-domain optical coherence vibration tomography system for measuring the natural frequency of cantilever beams and analyzing microstructure vibration modes[14].

The spatial-type OCT vibration measurement system can enhance performance by adding optical components, but it has a complex structure and is susceptible to external interference. Based on years of research on the ultra-small GRIN fiber probe composed sequentially of "single-mode fiber, no-core fiber, and GRIN fiber lens"[15,16], our research group has combined the ultra-small GRIN probe with fiber-based Swept Source OCT (SS-OCT) to study an integrated SS-OCT vibration measurement system model. Experimental measurements have verified the effectiveness of the fiber-based SS-OCT vibration measurement method. Additionally, by creating a MEMS fiber acoustic sensor, high-precision measurement of acoustic vibration signals has been achieved, expanding the application field of the SS-OCT system in vibration detection. The research above has validated the feasibility of the fiber-based SS-OCT vibration measurement model and method. However, it has not explored the factors affecting the system's displacement resolution and the methods to improve it, which is crucial for effectively utilizing OCT's high-resolution advantage.

The displacement resolution of an SS-OCT system is determined by two critical factors: the spectral resolution of the Fourier-transformed interference signal and the frequency estimation accuracy of the spectral correction algorithm. While hardware-dependent spectral resolution imposes inherent limitations on system performance, enhancing frequency estimation accuracy emerges as the pivotal strategy for optimizing displacement resolution. Leveraging advancements in fiber-based SS-OCT vibrational metrology, this study investigates the quantifiable influence of spectral correction algorithm frequency estimation precision on displacement resolution and the functional relationship between estimation accuracy and interference signal SNR. Employing an All-Phase FFT spectral analysis framework with phase difference methodology, we implement a novel Kaiser-Hanning hybrid convolution window to mitigate spectral leakage artifacts. This approach demonstrably enhances displacement resolution in fiber-optic SS-OCT configurations. Comprehensive experimental validation involves micro-vibration signal detection in mechanical structures, with systematic evaluations confirming the efficacy and robustness of the methodology.

2 Methods

2.1 Vibration Measurement Principle

As illustrated in Fig. 1, the SS-OCT system utilizing an ultra-small GRIN fiber probe operates as a low-coherence Michelson interferometer with a swept source. The swept source emits a sweeping light beam, which is split into two beams by the beam splitter. Within the sample arm, the beam is focused and emitted by the ultra-small GRIN fiber probe, and the reflected light (signal light) containing the sample's vibration data interferes with the reflected light (reference light) from the reference arm in the fiber coupler. Analyzing the interference signal provides insight into the sample's vibrational characteristics.

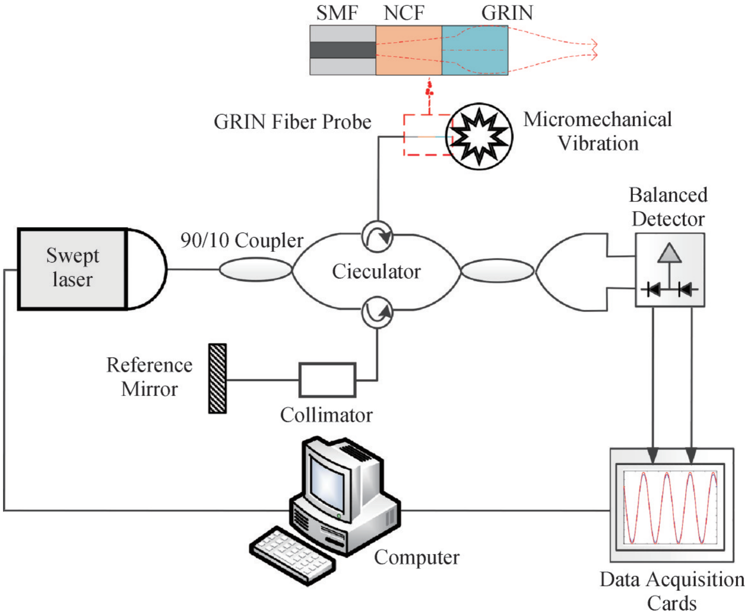

Fig.1 Diagram of SS-OCT vibration measurement system

The interference light intensity I is denoted as

$$I(k)=s(k)\left[R_r+R_z+2\sqrt{R_r}\cos(k\Delta L)\right] \tag{1}$$

where $s(k)$ is the spectral signal of the swept source, R_r is the reflectivity of the reference arm mirror, R_z is the reflectivity of the sample surface, and ΔL is the optical path difference between them. When the sample vibrates sinusoidally, the optical path difference ΔL(t) varies with time, causing the interference signal to be temporally modulated. The resulting modulation frequency corresponds to the vibration frequency of the sample. According to the Wiener-Khinchin theorem[17], applying FFT to the third term in Eq. 1 can convert the effective interference signal from wavenumber space k to depth space z. By resampling the effective interference signal at equal wavenumbers before applying the FFT, the FFT result is,

$$FFT\{I(k)\}=\Gamma(z)\otimes 2\sqrt{R_r R_z}\,\delta(z\pm\Delta L) \tag{2}$$

where $\Gamma(z)$ represents the Fourier transform output of the swept source $s(k)$, and z denotes the initial optical path discrepancy between the two arms. By adjusting z to 0, ΔL equals the optical path difference between the two arms during sample vibration. By utilizing Eq. 2, the position information of the sample can be obtained. Fundamentally, a Fourier transform correlation exists between the spectral and optical path signals. By applying a Fourier transform to the spectral signal, the optical path signal can be obtained, thereby achieving the measurement of displacement changes. Equation (1) shows that the frequency f of the interfering signal is positively correlated with the optical range difference ΔL. Thus the corresponding optical range difference can be calculated by the frequency value of the interfering signal. Each position corresponds to an oscillation frequency, where the frequency point f1 is recorded at zero optical path difference. Then, the rail at one end of the reference arm is adjusted to change the optical path difference, and the frequency f2 is recorded. This process establishes the link between frequency and optical path difference. By monitoring the interference signal of the reflected light from the vibrating object over a duration, the corresponding frequency can be deduced from the FFT output of the interference signal, translating it into the object's positional information at specific time instances. Through this position change, information over time can be obtained, allowing parameters such as the vibration frequency and amplitude of the sample to be determined.

2.2 Frequency Estimation Algorithm

The preceding analysis demonstrates that the SS-OCT system's ranging principle involves determining optical path difference information through precise measurement of interference signal frequency. This frequency corresponds directly to the position of the fundamental spectral peak. By tracking variations in this dominant spectral component, we can effectively monitor the frequency characteristics of the interference signal. Therefore, the spectral resolution obtained from the FFT-processed interference signal fundamentally determines the system's achievable displacement resolution.

As shown in Fig. 2, f_0, f_1, f_2, and f_3 represent the spectral line values in the frequency domain of the interference signal. f denotes the true spectral line of the interference signal, and the spectral resolution is denoted as Δf. The frequency of the interference signal obtained in the frequency domain diagram corresponds to the main spectral line f_2. If the frequency variation of the interference signal is below Δf, the main spectral line in the frequency domain diagram remains unchanged, thus rendering the system incapable of detecting the corresponding optical path difference alteration.

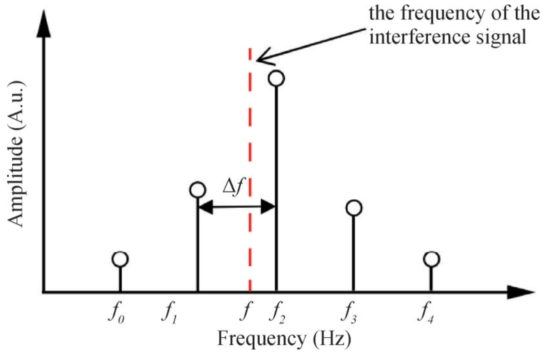

Fig. 2 Frequency domain diagram of interference signal

As can be seen from Eq. 1, the frequency of the interfering signal obtained in the frequency domain diagram is the corresponding frequency value of the main spectral line f_2, when the frequency change of the interfering signal is less than Δf, the main spectral line in the frequency domain diagram will not change, so the system can not detect the corresponding change in the optical range difference. In this study, a swept source model HSL20-50-B produced by Japan's Santec Corporation, operating at a frequency of 50 kHz, is utilized. The center wavelength λ_0 is 1300.4 nm and the spectral bandwidth $\Delta\lambda$ is 106.3 nm for the HSL-20-50-B swept light source produced by the Japanese company Santee. Δf corresponds to an optical range difference change Δz of 7 μm, thereby somewhat constraining the SS-OCT's capacity to identify submicron to nanometer-scale displacement variations.

Spectral correction technology is a general term for methods that obtain the signal's frequency, amplitude, and phase through a discrete spectrum. By combining spectral correction technology with OCT ranging technology, accurate estimation of the interference signal frequency can be achieved, effectively improving the displacement resolution of the OCT system. The improvement in displacement resolution depends on the estimation accuracy of the frequency estimation algorithm. Let the estimation accuracy of the frequency estimation algorithm be ε, and let the optical path difference corresponding to the spectral resolution be Δz. The displacement resolution of the SS-OCT system can be expressed as,

$$\Delta d=\varepsilon\Delta z \tag{3}$$

Frequency estimation algorithms determine signal frequency via discrete spectral analysis, where signal noise profoundly impacts spectral characteristics. The SNR of interference signals directly determines the precision of frequency estimation. Common methods, such as phase difference, energy centroid, and ratio techniques, each have distinct limitations. The energy centroid and ratio methods employ mathematical approximations that compromise accuracy, with errors in the ratio method tied to the length of the window function and energy centroid deviations dependent on the spectral line count. By contrast, phase difference methods assess frequency through temporal phase shift analysis of identical spectral lines, providing unbiased and high-precision estimates in noise-free scenarios.

This analysis underscores the critical role of precise spectral line data in achieving high-accuracy interferometric frequency estimation. Spectral line parameters such as phase and amplitude are primarily influenced by two factors: interferometric signal SNR and spectral leakage. This work addresses these two aspects to enhance frequency estimation precision and improve system displacement resolution.

3 Method for Improving Displacement Resolution

3.1 SNR Improvement of the Interference Signal

The SNR in the SS-OCT system is defined as the ratio of the square of the interferometric signal light intensity value, I^2, to the noise variance, $\sigma^2{}_{\text{noise}}$, which can be expressed as

$$SNR = 10\log\left(\frac{I^2}{\sigma^2_{noise}}\right) \tag{4}$$

Noise mainly consists of thermal noise, scattered particle noise, and relative intensity noise. When the reference optical power is sufficiently large, after the photoelectric balance detector filters out the noise, the remaining noise is primarily scattering noise. For convenience of calculation, the expression for the SNR of the SS-OCT system can be simplified by replacing the noise variance with the scatter-grain noise, and the expression for the SNR of the SS-OCT system can be simplified as

$$SNR = \frac{\eta\tau}{hv}P_{\text{s}} \tag{5}$$

where P_s is the sample light optical power received by the sample arm, η is the quantum efficiency, h denotes Planck's constant, v is the propagation frequency of light, and τ is the integration time of the photoelectric balance detector.

From Eq. 5, it is evident that enhancing the received optical power can effectively enhance the SNR of the interference signal. Single-mode fiber dispersion leads to a decrease in received optical power with an increase in sample vibration displacement. To enhance the focusing performance of the outgoing light, this paper introduces the design and fabrication of an all-fiber-type self-focusing probe comprising a single-mode fiber, a coreless fiber, and a GRIN fiber fused sequentially. The coreless fiber is utilized for beam expansion, overcoming the limitations of small mode field diameter and short working distance in single-mode fiber. The GRIN fiber is employed to focus the output beam. The structure of the self-focusing probe is illustrated in Fig. 3.

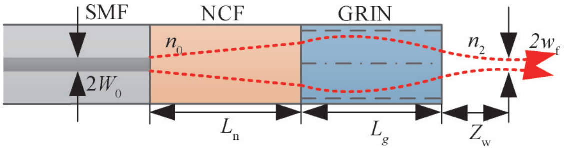

Fig. 3 Structure diagram of a self-focusing fiber optic probe

To meet the system's millimeter-level amplitude detection requirements, a self-focusing fiber probe was fabricated by fusion-splicing a 0.36-mm-long coreless fiber with a 0.1-mm-long GRIN fiber. The probe's working distance Z_w is 0.76 mm, with a focusing spot diameter $2w_f$ of 32 µm. In fiber-based OCT systems, the received optical power depends on the probe's coupling efficiency. For single-mode probes, this efficiency decreases as the distance between the probe and the sample increases[18]. The coupling efficiency of a self-focusing probe that focuses first and then diverges can be expressed as

$$\eta = \frac{P_s}{P} = 1 - \exp\left\{-\frac{R^2}{2w_f^2 + 2\left[\frac{\lambda}{\pi w_f}(2z - Z_w)\right]^2}\right\} \tag{6}$$

P represents the outward optical power, and R stands for the core radius of the GRIN fiber probe, set at 25 µm. By inserting the working distance Z_w of the self-focusing probe and the focusing spot radius w_f into (6), the correlation between the coupling efficiency of the GRIN probe and the distance z between the sample and the probe is illustrated in Fig. 4. The coupling efficiency initially rises as the distance increases, then decreases, reaching its peak when the spacing equals half the working distance.

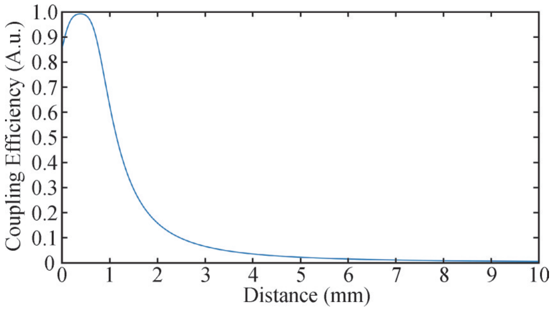

Fig. 4 The relationship between the coupling efficiency of a self-focusing fiber probe and the distance between the sample and the probe

Using a 1-mm amplitude as the analytical benchmark, Fig. 4 demonstrates that the coupling efficiency of the self-focusing fiber probe exhibits a non-monotonic trend within the 1-mm range—initially increasing, then decreasing. Consequently, the probe's optical power reception follows this pattern, with the corresponding interference signal SNR reaching its minimum value at the 1-mm endpoint. When evaluated at a 1-mm displacement (Fig. 5), the self-focusing fiber probe achieves an interference signal SNR of 42 dB, whereas a conventional single-mode fiber yields only 31 dB under identical conditions. This represents an 11 dB improvement in signal quality, underscoring the probe's enhanced light-gathering capability. Notably, the analysis confirms that the self-focusing fiber probe maintains an SNR exceeding 40 dB across the entire 1 mm amplitude range. This ensures robust signal integrity even at maximum displacement, validating its suitability for high-resolution sensing applications where displacement amplitudes approach the millimeter scale.

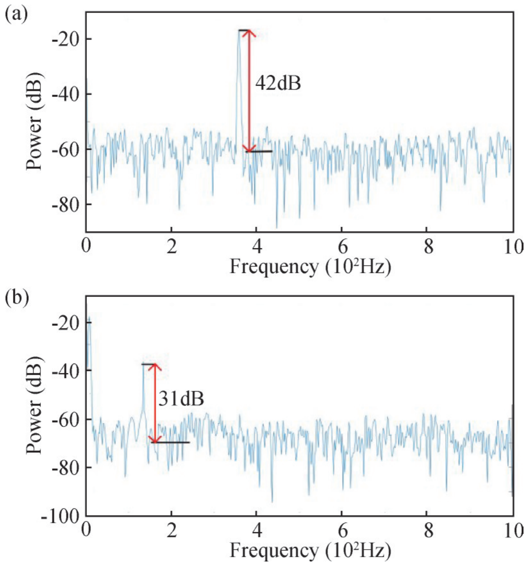

Fig. 5 SNR of interference signals at a 1mm spacing. (a) self-focusing fiber probe,(b) single-mode fiber probe

3.2 All-phase FFT Spectral Analysis Phase Difference Method

The phase difference method demonstrates superior frequency estimation performance, yet its dependency on discrete spectral data derived from the FFT renders its accuracy vulnerable to spectral leakage artifacts. Mitigating such leakage is critical to achieving enhanced frequency estimation precision. This study proposes a principle-driven approach to suppress spectral leakage in FFT-based analysis through all-phase data preprocessing, thereby elevating estimation accuracy. The All-phase FFT (Taking the example) technique[19] operates by systematically time-shifting the input signal across its entire duration and synthesizing these shifted versions to attenuate truncation-induced errors. This preprocessing framework theoretically minimizes Gibbs phenomenon-related distortions, as schematically outlined in Fig. 6. By aggregating spectral information from cyclically permuted signal segments, the AP-FFT algorithm achieves better spectral leakage suppression and phase invariance compared to conventional FFT methods, particularly in applications where signal edges contain critical spectral content.

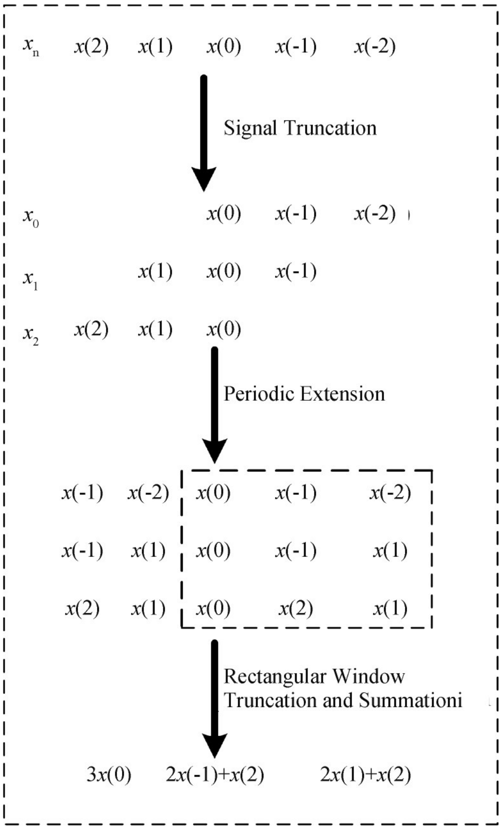

Fig. 6 All-phase FFT processing flow

Let $\{x(n)=e^{j(\theta+2\pi n\beta/N)}\}$ be the discrete sequence of a single-frequency complex exponential signal. Applying a rectangular window to truncate x(n), its DFT expression is shown in Eq. 7. If the same rectangular window truncation is used for AP-FFT processing, the resulting spectral expression is described by Eq. 8. Here, $2\pi\beta/N$ denotes the discrete signal frequency, and θ is the initial phase of the discrete signal. From Eqs. 7 and 8, it can be seen that the corresponding amplitude of the same position spectral line in AP-FFT is the square of the corresponding amplitude in FFT. In the spectral diagram, the amplitude corresponding to the signal peak is much larger than the amplitude of the side spectral lines.

After squaring the amplitudes, more energy is concentrated in the main spectral line. Therefore, AP-FFT can achieve better spectral leakage suppression compared to FFT.

$$\begin{aligned} X(k) &= \frac{e^{j\theta}}{N}\sum_{n=0}^{N-1} e^{-j(k-\beta)\frac{2\pi}{N}n} \\ &= \frac{e^{j\theta}}{N}\frac{1-e^{j2\pi(\beta-k)}}{1-e^{j2\pi(\beta-k)/N}} \\ &= \frac{1}{N}\frac{\sin[(\beta-k)\pi]}{\sin[(\beta-k)\pi/N]}e^{j[\theta+(1-\frac{1}{N}(\beta-k)\pi)]} \end{aligned} \tag{7}$$

$$\begin{aligned} X_{ap}(k) &= \frac{1}{N}\sum_{i=0}^{N-1}\sum_{n=0}^{N-1} x(n-i)e^{-j\frac{2\pi}{N}kn}e^{j\frac{2\pi}{N}ki} \\ &= \frac{e^{j\theta}}{N^2}\sum_{n=0}^{N-1} e^{-j\frac{2\pi(\beta-k)i}{N}}\sum_{n=0}^{N-1} e^{j\frac{2\pi(\beta-k)n}{N}} \\ &= \frac{e^{j\theta}}{N^2}\frac{\sin^2[(\beta-k)\pi]}{\sin^2[(\beta-k)\pi/N]} \end{aligned} \tag{8}$$

For the fiber-based SS-OCT vibration measurement system, the SNR of the collected interference signal is affected by the sample's vibration amplitude, with the SNR ranging from 30 dB to 40 dB. The SNR is set to 35 dB and 40 dB, and the signal frequency is incremented from 15.50 Hz to 16.49 Hz with a step size of 0.01 Hz. Where N is the length of the window function and takes the value 3. A Hanning window is used to truncate the signal, where the window function length is 1024, and the sampling frequency is 1024 Hz. The phase difference method and the AP-FFT spectral analysis phase difference method are used to estimate the signal frequency, and the estimation errors are shown in Fig. 7. In the figure, the horizontal axis represents the frequency offset, and the vertical axis represents the logarithm (base 10) of the relative error. As seen in Fig. 7, as the SNR of the signal decreases, the frequency errors calculated by both methods increase, but the error from the AP-FFT method is significantly smaller. For signals with the same SNR, the calculation accuracy of the AP-FFT is nearly 20% higher than that of the FFT. Moreover, the higher the SNR, the better the estimation performance of the AP-FFT. When the SNR reaches 40 dB, the frequency estimation error using the AP-FFT spectral analysis phase difference method is less than 10^{-4}. Substituting the frequency estimation accuracy of the all-phase FFT spectral analysis phase difference method into equation (3), the displacement resolution of the fiber-based SS-OCT system can be calculated to be approximately 1 nm.

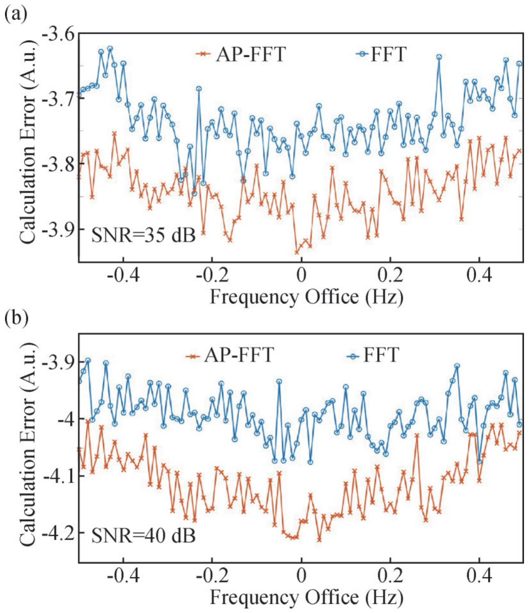

Fig. 7 Frequency calculation errors of different frequency offsets. (a) SNR=35 dB, (b) SNR=40 dB.

3.3 Kaiser-Hanning Hybrid Convolution Window Design

Spectral leakage occurs due to the irregular truncation of signals. While using a window function to truncate the signal, spectral leakage is unavoidable. Various window functions differ in their ability to reduce spectral leakage. Enhancing window functions to minimize spectral leakage can enhance the accuracy of frequency estimation in the AP-FFT spectral analysis phase difference method. The key factors of window functions are the width of the main lobe and the performance of the side lobes, which influence each other. Window functions with narrow main lobes concentrate spectral leakage in the side lobes, leading to high side lobe leakage. On the other hand, window functions with low side lobe leakage have spectral leakage mainly within the main lobe, resulting in a broader main lobe. Therefore, when selecting a window function, it's crucial to strike a balance between having a small main lobe width, low side lobe peak level, and high side lobe attenuation rate.

The paper proposes a Kaiser-Hanning hybrid convolution window design to achieve a narrower main lobe width and a quicker attenuation rate in the side lobes. The Kaiser window comprises configurable zero-order Bessel functions. By adjusting β, the ratio between the main lobe's amplitude and the side lobe's amplitude can be flexibly tuned to prioritize the signal. The time-domain expression is as follows,

$$\omega_K(n)=\frac{I_0\left[\beta\sqrt{1-\left(\frac{n-N/2}{N/2}\right)^2}\right]}{I_0(\beta)},0\le n\le N \qquad (9)$$

As β increases, the side lobe level decreases while the width of the main lobe gradually increases. When β is set to 11, the Kaiser window is convolved with the Hanning window. By setting the length of the window function to 64, the amplitude-frequency characteristics of the Hanning window, Kaiser window, first-order Hanning self-convolution window, and Kaiser-Hanning hybrid convolution window are plotted (as shown in Fig. 8). The performance of the two convolution windows is significantly improved compared to the Hanning window. With the same main lobe width, they demonstrate a lower side lobe peak level and side lobe attenuation rate. In comparison to the Kaiser window with $\beta = 11$, the Kaiser-Hanning hybrid convolution window has a slightly higher side lobe peak level but significantly better main lobe width and side lobe attenuation rate, resulting in superior overall performance. When contrasted with the Hanning self-convolution window, the hybrid convolution window possesses an approximately equal main lobe width, slightly higher side lobe peak level, and notably better side lobe attenuation rate.

Using the Kaiser-Hanning hybrid convolution window for the AP-FFT spectral analysis phase difference method, the single-frequency sinusoidal signal frequency is set to 15 Hz, the window function length is 128, and the sampling frequency is 128 Hz. Setting the SNR at 25 dB, 30 dB, 35 dB, and 40 dB, respectively, and 1000 signals for obtaining the average estimation

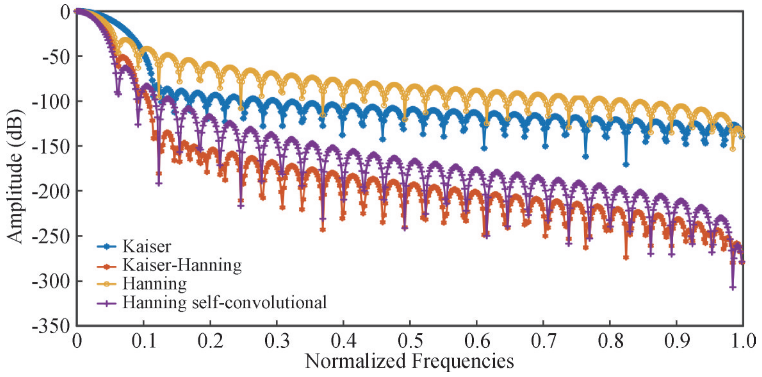

Fig. 8 Amplitude and frequency characteristics of different window functions

error. The frequency estimation errors for the Kaiser-Hanning hybrid convolution window and the Hanning self-convolution window are illustrated in Table 1. The Kaiser-Hanning hybrid convolution window demonstrates superior ability in suppressing spectral leakage for single-frequency signals. Across different SNRs, the frequency estimation accuracy of the AP-FFT spectral analysis phase difference method utilizing the Kaiser-Hanning hybrid convolution window shows enhancements ranging from 5% to 15%.

Table 1 Frequency estimation error under different SNRs for different window functions

Window functions	20dB	30dB	30dB	40dB
Hanning self-convolution window	4.7e-4	2.7e-4	1.5e-4	8.4e-5
Kaiser-Hanning hybrid convolution window	4.5e-4	2.5e-4	1.3e-4	8.0e-4

4 Experiment

4.1 Nano-Scale Vibration Detection with a Displacement Stage

To optimize the utilization of reflected optical power for enhancing the SNR of the interference signal, a novel ultra-compact GRIN fiber probe was designed and fabricated. This probe integrates a 0.36-mm-long coreless fiber segment with a 0.1-mm-long GRIN fiber segment via fusion splicing. The operational distance Z_w is 0.76 mm, and the diameter of the focused spot $2w_f$ is 32 μm. Through an assessment of the coupling effectiveness of the ultra-small GRIN fiber probe[18], the coupling efficiency can exceed 40% within a 1 mm amplitude range, leading to an SNR of the obtained interference signal surpassing 40 dB. As per the aforementioned analysis, with an SNR of 40 dB, the error in frequency estimation using the AP-FFT phase difference technique with a hybrid convolution window is less than 10^{-4}. By substituting this value into Eq. 3, the resolution for displacement can achieve 1 nm. The operational concept of the SS-OCT vibration measurement system is depicted in Fig. 1.

Using a nano-displacement stage, a 100 Hz sinusoidal vibration was induced with an amplitude of 0.1 μm. The system recorded 1000 data points in 40 ms, with a stage displacement difference of approximately 1 nm between each data point. The vibration signal was captured using a fiber-based SS-OCT system. The interference signal frequency was determined through phase difference analysis, and the resulting plot is depicted in Fig. 9.

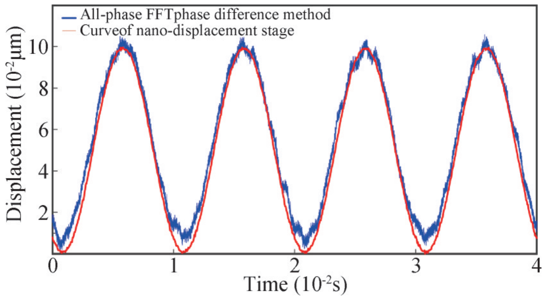

Fig. 9 System test result of 0.1 μm vibration signal

The frequency estimation using the AP-FFT spectral analysis method closely matched the actual vibration pattern of the nano-positioning stage, except for minor discrepancies at peak vibrations. This discrepancy arises from minimal displacement differences at peak data points, leading to a higher estimation error in the phase difference method compared to the frequency fluctuation of the interference signal. Consequently, the SS-OCT system, utilizing the AP-FFT spectral analysis phase difference method, achieves nanometer-level displacement resolution, facilitating precise vibration detection.

4.2 Comparison with Laser Self-Mixing Interferometry

Taking the example of capturing the vibration signal from a micro-motor shaft, we have validated the potential of the fiber-based SS-OCT system for detecting micro-mechanical vibrations. To detect the vibration signal of a small motor's shaft, we first validated the feasibility of SS-OCT for detecting vibration signals from high-speed rotating objects. Laser self-mixing vibration measurement technology is a mature and high-precision optical vibration detection technology. By using both the SS-OCT system and a laser self-mixing interferometer to detect the axial vibration of the same motor shaft, we verified the measurement accuracy of the fiber-based SS-OCT system. The experiment used a laser self-mixing interferometer, model HFE4093-332 from Finisar Corporation. This system can precisely reconstruct vibration curves of an external reflector at the nanometer level, with device nonlinearity and hysteresis both below 1%.

The axial vibration of the 37GB555 DC gear motor shaft was detected using both methods. Operating at 100 revolutions per minute, the motor had a shaft length of 15 mm, a circumference diameter of 6 mm, and a milled edge face of 5.5 mm. The measurement results of the two techniques during normal motor operation are illustrated in Fig. 10. The laser self-mixing interferometer sampled 4.2×10^5 points in 6.2 seconds due to its sampling settings, as depicted in the time-domain signal in Fig. 10(a). On the other hand, the SS-OCT system acquired 1000 points in 0.04 seconds with a sampling frequency of 25000 Hz, thus achieving a frequency resolution of 24.4 Hz. As shown in Fig. 10, the results from the SS-OCT system reveal that the axial vibration frequency of the motor shaft falls between 98 Hz and 122 Hz. Via the previously outlined spectral correction method, the true frequency was adjusted to 112 Hz, exhibiting an amplitude of 0.56 µm. To conclude, the results from both methods demonstrate high consistency, indicating the viability of utilizing the SS-OCT system for shaft vibration analysis.

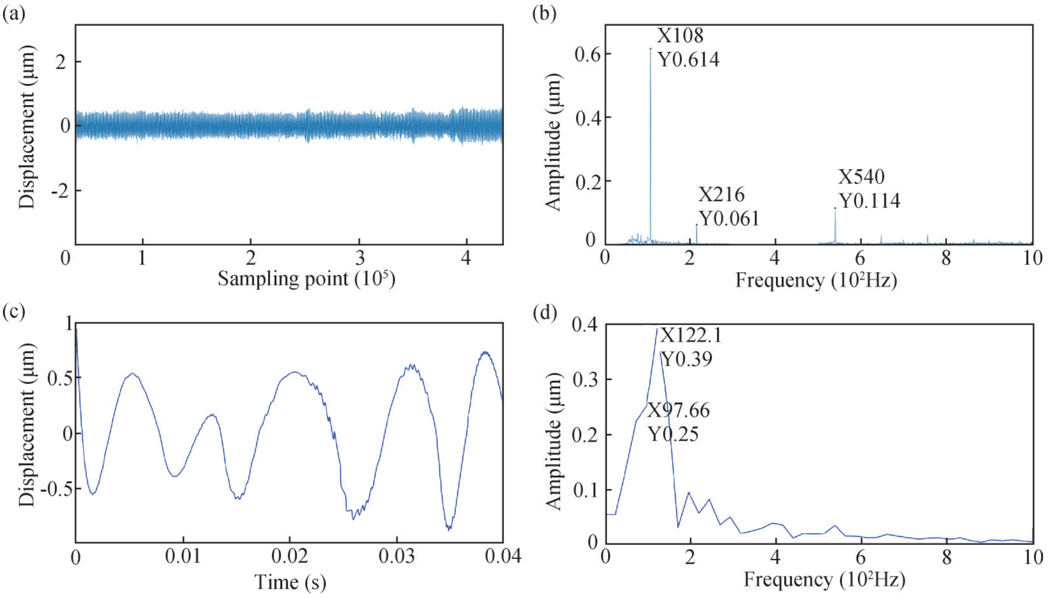

Fig. 10 Axial vibration test results of 6mm motor shaft. (a) laser self-mixing interferometer time-domain signal. (b) laser self-mixing interferometer frequency-domain signal. (c) SS-OCT system time-domain signal. (d) SS-OCT system frequency-domain signal.

4.3 Micro-Motor Shaft Damage Detection Using SS-OCT

In the above experiment, the feasibility of the fiber-based SS-OCT system for measuring vibration signals of rotating shafts was confirmed by comparing the results with a laser self-mixing interferometer. An example using a 716 coreless motor to detect micro-motor shaft vibrations was presented. The 716 coreless motor, with dimensions of 7 mm in diameter and 16 mm in length, a shaft diameter of 0.8 mm, a rated voltage of 3.4 V, and a maximum rotational speed of 34,000 r/min, was utilized. Unlike the laser self-mixing interferometer, which has a large output beam, the fiber-based SS-OCT system, with its small sample arm probe size, effectively captures the micro-motor shaft's vibration signal, showcasing its advantages and application value in micro-mechanical vibration detection.

After supplying the motor with a rated voltage of 3.4 V and allowing it to reach a stable state, runout detection was performed. The axial runout of the motor shaft was measured both under idle and loaded conditions. During operation, the motor shaft was deliberately impacted with the table to create a bend at a specific angle. Subsequently, the damaged motor was powered normally, and the axial runout of the motor shaft was reevaluated under both idle and loaded conditions. The measurement outcomes are illustrated in Fig. 11.

The experimental findings suggest that the axial runout of the motor shaft increased significantly after the damage. The primary frequency of the idle vibration signal shifted to 1093 Hz, showing minimal deviation

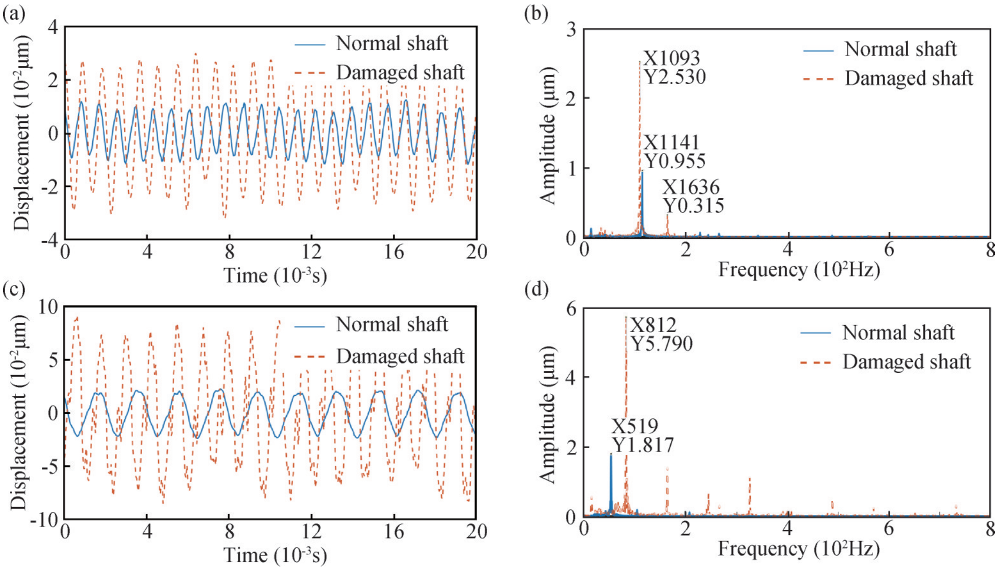

Fig. 11 Axial vibration signal of micromotor before and after shaft damage. (a) idle time-domain signal, (b) idle frequency-domain signal, (c) loaded time-domain signal, (d) loaded frequency-domain signal.

from the pre-damage vibration frequency. However, the vibration amplitude surged to about 2.5 μm. Contrarily, the loaded vibration signal exhibited substantial alterations after the damage, with the main vibration frequency adjusting to 812 Hz, akin to the pre-damage condition. Moreover, there were prominent noise elements at double and quadruple the main frequency, along with evident noise components at six and eight times the main frequency. The vibration amplitude of the post-damage vibration signal increased to around 6 μm, three times the amplitude before the damage.

5 Conclusion

This study investigated methods to improve the displacement resolution of the fiber-based SS-OCT vibration measurement system. By integrating the All-phase FFT spectral analysis phase difference method with the system, a Kaiser-Hanning hybrid convolution window with effective spectral leakage suppression was developed. This innovation enabled the precise estimation of the interference signal frequency, resulting in improved displacement resolution. An ultra-compact GRIN probe was engineered, boosting the interference signal's SNR to 40 dB. With this improved SNR, the frequency estimation error was below 10^{-4}. Calibration using a nano-displacement stage confirmed that the system could achieve nanometer-level displacement resolution in optimal conditions. The fiber-based SS-OCT vibration measurement system was then employed to monitor the axial vibration of a 0.8 mm diameter micromotor shaft. The system accurately detected the rise in axial vibration amplitude from 2 μm to 6 μm under load post-damage to the motor shaft, effectively distinguishing between the pre-damage and post-damage vibration signals. This showcases the potential utility of the fiber-based SS-OCT system in detecting mechanical damage.

Author Contribution:

Famin Wang: Conceptualization; Formal analysis; Writing-review & editing; Yongyi Tan: Data curation; Writing-original draft; Jingyi Gu: Data curation; Jiao Li: Funding acquisition; Resources; Chi Wang: Funding acquisition; Project administration; Resources.

Acknowledgments:

The authors are grateful to thank the State Key Laboratory of Precision Measurement Technology and Instruments for their support.

Funding Information:

This research was funded by the National Natural Science Foundation of China (NSFC) (62405174); State Key Laboratory of Precision Measurement Technology and Instruments (Pilab2402); and Fundamental Research Funds for the Central Universities (3122016C010).

Data Availability:

The authors declare that the main data supporting the findings of this study are available within the paper.

Conflicts of Interest:

The authors declare no competing interests.

Dates:

Received 31 March 2025; Accepted 25 August 2025; Published online 30 September 2025

References

[1] P. Mlyniuk, et al., (**2024**). Air-puff induced corneal dynamics in normal, forme fruste and keratoconic eyes measured with

OCT-based optical biometry[J], *Opt. Lasers Eng.* , 176, Page 108124.

[2] M. A. Urbańska, et al., (**2024**). OCT-based dynamic mechanical analysis of vitreous humour[J], *Opt. Lasers Eng.* , 172, Page 107881.

[3] Z. Alam, et al., (**2022**). An in-vivo depth-resolved imaging of developing zebrafish microstructure and microvasculature using swept-source optical coherence tomography angiography[J], *Opt. Lasers Eng.* , 156, Page 107087.

[4] M. Bhende, et al., (**2018**). Optical coherence tomography: A guide to interpretation of common macular diseases[J], *Indian. J. Ophthalmol.* , 66(1), Page 20-35.

[5] F. Wang, et al., (**2024**). Single-molecule tracking technology based on symmetric power exponential phases[J], *Opt. Lett.* , 49(20), Page 5870-5873.

[6] J. Qin, et al., (**2021**). Optical coherence tomography for ophthalmology imaging[J], *Adv. Exp. Med. Biol.* , 3233, page 197-216.

[7] S. W. F. Meenderink, et al., (**2022**). Organ of Corti vibrations are dominated by longitudinal motion in vivo[J]. *Commun. Biol.* , 5(1), Page 1285-1291.

[8] B. Zhang, et al., (**2024**). RC-Net: A region-level context network for hyperreflective dots segmentation in retinal OCT images[J]. *Opt. Lasers Eng.* , 172, Page 107872.

[9] X. Zhang, et al., (**2024**). Depth-resolved stress field measurement of multilayered system using swept-source polarization-sensitive optical coherence tomography[J], *Opt. Lasers Eng.* , 178, Page 108215.

[10] F. Wang, et al. (**2024**). Ring-shaped segmentation phase design method for the combined point spread function[J], Opt. *Express.* , 32(17), Page 29014-29029.

[11] S. Zhong, et al., (**2015**). Enhanced optical coherence vibration tomography for subnanoscale- displacement-resolution calibration of piezoelectric actuators[J], *Sensor Actuat A-Phys.* , 233, Page 42-46.

[12] Q. Zhang, et al., (**2020**). Anti-noise frequency estimation performance of Hanning-windowed energy centrobaric method for optical coherence velocimeter[J], *Opt. Lasers Eng.* , 134, Page 106250.

[13] F. Wang, et al., (**2023**). Double helix point spread function with variable spacing for precise 3D particle localization[J], *Opt. Express.* , 31(7), Page 11680-11694.

[14] N. Zhou, et al., (**2018**). Acoustic-excitation based on optical coherence vibration tomography for modal analysis of microbeams[J], *IEEE T Instrum Meas.* , 69(9), Page 7209-7217.

[15] C. Wang, et al., (**2016**). Measurement of the focusing constant of gradient-index fiber lens and its application in developing GRIN fiber probes[J], *MEAS.* , 90, Page 542-548.

[16] C. Wang, et al., (**2016**). A novel integrated fiber-optic interferometer model and its application in micro-displacement measurement[J], *Opt. Lasers Eng.* , 86, Page 125-131.

[17] Y. Chen, et al., (**2022**). Quantum Wiener-Khinchin theorem for spectral-domain optical coherence tomography[J], *Phys. Rev. Applied.* , 18(1), Page 014077.

[18] C. Wang, et al., (**2017**). Coupling efficiency of ultra-small gradient-index fiber probe[J], *Opt. Commun.* , 389, Page 265-269.

[19] K. Kou, et al., (**2021**). All-phase FFT based distance measurement in laser self-mixing interferometry[J], *Opt. Lasers Eng.* , 142, Page 106611.